

# Structural Study of Carbon-Coated TiO<sub>2</sub> Anatase Nanoparticles as High-Performance Anode Materials for Na-Ion Batteries

Giorgia Greco,<sup>\*,†,‡</sup> Katherine A. Mazzio,<sup>†,‡</sup> Xinwei Dou,<sup>‡,§</sup> Eike Gericke,<sup>†,||</sup> Robert Wendt,<sup>†,‡</sup> Michael Krümmey,<sup>‡</sup> and Stefano Passerini<sup>\*,‡,§,||</sup>

<sup>†</sup>Helmholtz-Zentrum Berlin für Materialien und Energie GmbH (HZB), Hahn-Meitner-Platz 1, D-14109 Berlin, Germany

<sup>‡</sup>Helmholtz Institute Ulm (HIU), Helmholtzstr. 11, 8901 Ulm, Germany

<sup>§</sup>Karlsruhe Institute of Technology (KIT), P.O. Box 3640, 76021 Karlsruhe, Germany

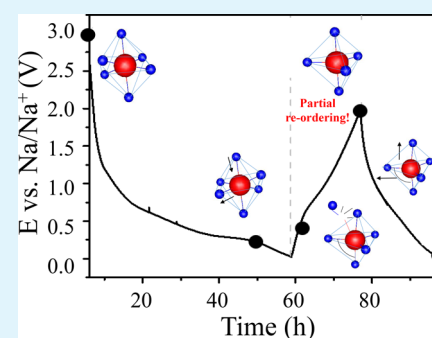
<sup>||</sup>Institut für Chemie, Humboldt-Universität zu Berlin, Brook-Taylor-Str. 2, D-12489 Berlin, Germany

<sup>‡</sup>Physikalisch-Technische Bundesanstalt (PTB), Abbestr. 2-12, D-10587 Berlin, Germany

## Supporting Information

**ABSTRACT:** In this work, we study the electronic and atomic structural modifications occurring in TiO<sub>2</sub> anatase nanoparticles as anode materials in Na-ion batteries upon sodiation and desodiation. The structural investigation is performed over both long- and short-range order by combining a comprehensive extended X-ray absorption fine structure (EXAFS) characterization with X-ray diffraction (XRD). The evolution of the electronic structure upon cycling is qualitatively investigated by X-ray absorption near-edge structure (XANES) analysis. The goal of this work is to correlate the outstanding electrochemical performance of carbon-coated TiO<sub>2</sub> anatase nanoparticles in sodium batteries with the electronic and structural modifications induced during the sodiation and desodiation processes upon cycling. This work also demonstrates for the first time a coherent explanation of the structural changes observed, where an electrochemically induced short-range ordering is revealed upon cycling.

**KEYWORDS:** sodium batteries, TiO<sub>2</sub> nanoparticles, EXAFS, XANES, SAXS, structural characterization



Sodium-ion batteries (SIBs) are one of the most promising complementary candidates to lithium-ion batteries (LIBs) because of the high abundance of the raw materials employed. Additionally, they share the same working principles and cell structures of LIBs, thus benefiting from previously developed cell-making technologies. Due to these inherent benefits, SIBs are envisioned for use in applications related to large-scale energy storage systems and other applications not requiring top performance.<sup>1–6</sup> Compared with other “beyond LIB” chemistries, such as potassium-ion batteries (PIBs) and magnesium-ion batteries (MIBs), SIBs are mostly close to commercialization.<sup>7–10</sup> However, to fully accomplish market deployment, suitable anode materials are still needed. Unfortunately, both graphite, which is the most widely used anode material in LIBs, and silicon, which is foreseen as the next-generation anode for LIBs, do not show a very promising electrochemical performance in SIBs.<sup>11–13</sup> Among the most promising anode materials, hard carbons are the most studied because of their extremely good sustainability, abundance, cost, and performance characteristics.<sup>14</sup> However, hard carbons suffer due to safety issues related to the Na<sup>+</sup>-ion storage mechanism, which exhibits a long plateau at low voltages that are only slightly above the sodium metal plating potential. Thus, sodium metal plating may easily occur, which raises safety concerns when used in conjunction with volatile,

organic, carbon-based electrolytes.<sup>15,16</sup> Due to its higher operating voltage, TiO<sub>2</sub> has been gaining attention as an anode material despite its relatively low sodium storage capacity compared to hard carbons. TiO<sub>2</sub> is abundant and low-cost and, most importantly, does not suffer from sodium plating during cycling.<sup>17–19</sup> In previous work, it has been demonstrated that the production technique, particle size, and carbon coating strongly influence the electrochemical performance of TiO<sub>2</sub> in SIBs.<sup>20</sup> In particular, the carbon-coated TiO<sub>2</sub> nanomaterials developed by Tahir et al.<sup>20</sup> show extraordinary performance in terms of specific capacity (up to 227 mA h g<sup>-1</sup>), rate capability, stability, and efficiency (≈99.8%).

In this work, we follow the electrochemical Na<sup>+</sup>-ion storage mechanism in this high-performance material. The Na<sup>+</sup> insertion in TiO<sub>2</sub> occurs after an initial activation that includes structural transformations, which are comprehensively investigated herein by combining X-ray diffraction (XRD) and small-angle X-ray scattering (SAXS) with X-ray absorption spectroscopy (XAS). The combination of these techniques gives a complete overview of the electronic and atomic structural modifications along with the electrochemical

Received: June 4, 2019

Accepted: September 6, 2019

Published: September 6, 2019

behavior of the active material. The first part of this Article is devoted to the characterization of the pristine material and commercially available nanoparticles to establish the structural long-range order (LRO), nanoparticle dimensions, carbon coating characteristics, and the morphology. In the following sections, detailed results are reported from the comprehensive XAS characterization of the short-range order (SRO) of the  $\text{TiO}_2$  material both as a pristine powder and incorporated into composite electrodes. The structural modifications induced by sodiation of the composite electrodes are also investigated.

During the first sodiation, a large fraction of the charge does not correspond to  $\text{Na}^+$ -ion storage in the  $\text{TiO}_2$  structure but is rather consumed by the occurrence of irreversible reactions, including the formation of the solid electrolyte interphase (SEI) formed by the reduction of the electrolyte components.<sup>17,21</sup> However, an irreversible transformation of the  $\text{TiO}_2$  structure is observed, which may contribute to the irreversible behavior. A complete amorphization after the first sodiation along with an electronic structural rearrangement is observed. During the first desodiation the  $\text{TiO}_2$  atomic and electronic structure shows a clear electrochemically induced partial reordering, which well matches with the only partially reversible electrochemical behavior during the first sodiation/desodiation cycle. This work provides the first full characterization of the electronic and atomic structure alongside the electrochemical performance of  $\text{TiO}_2$  nanomaterials in SIBs.

## RESULTS AND DISCUSSION

**Sample Description.** The samples investigated consist of carbon-coated  $\text{TiO}_2$  anatase nanoparticles (labeled as C- $\text{TiO}_2$  NPs) synthesized and processed as previously reported.<sup>20</sup> For the sake of comparison, commercial  $\text{TiO}_2$  anatase NPs (labeled as  $\text{TiO}_2$  NPs, obtained from Sigma-Aldrich and used as received) were also investigated. Figure S1 shows the typical sodiation–desodiation behavior of an electrode composed of C- $\text{TiO}_2$  NPs. For the *ex situ* characterization, several cells were assembled and stopped at different degrees of sodiation within the first and second cycles at the points indicated in Figure S1. These include the pristine sample ( $S_0$ ) and after sodiation to 0.3 V ( $S_1$ ), desodiation to 0.4 V ( $S_2$ ) and 2.0 V ( $S_3$ ), and full sodiation ( $S_4$ ).

**Pristine C- $\text{TiO}_2$  and Commercial  $\text{TiO}_2$  Nanocrystal Characterization.** To obtain a detailed XAS data evaluation for understanding the evolution of the structural modifications induced by sodiation, it is crucial to characterize *a priori* the samples under study. Information such as the particle size, size distribution, and crystalline structure is required to obtain a comprehensive and reliable extended X-ray absorption fine structure (EXAFS) analysis.<sup>22–25</sup>

High-resolution transmission electron microscopy (HRTEM) and X-ray diffraction (XRD) were previously used to characterize the quasispherical shape and anatase phase structure of the materials under investigation, the details of which have been previously reported.<sup>20</sup> XRD scans for the reference  $\text{TiO}_2$  NPs (Sigma-Aldrich) and the carbon-coated C- $\text{TiO}_2$  NPs are presented in Figure S2a,b, respectively. The XRD scans demonstrate the typical anatase structure for both samples. The formal structure of  $\text{TiO}_2$  anatase is triclinic with 31 atoms in the primitive cell, as shown in Figure 1a, and having the following lattice parameters:  $a = b = 0.380$  nm and  $c = 0.961$  nm, with angles  $\alpha = \beta = \gamma = 90^\circ$ . The results obtained from Rietveld refinement are shown in Table 1. The lattice parameter  $c$  was found to be shorter than the theoretical value,

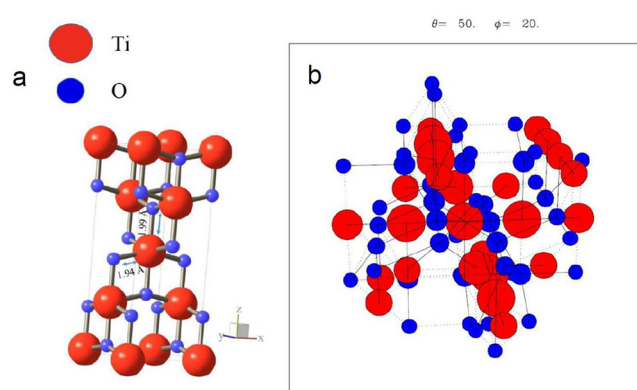


**Figure 1.** Ball and stick models of the  $\text{TiO}_2$  anatase structure: (a) primitive cell and (b) atomic cluster.

which is probably due to the nanosize of the samples. The nanoparticle size was evaluated according to the Debye–Scherrer equation<sup>26</sup> from the two most intense peaks, and SAXS measurements were used to confirm the actual size and size distribution.

Figure 2a provides the SAXS profile for the C- $\text{TiO}_2$  NPs, while Figure S3a shows that of the uncoated  $\text{TiO}_2$  NPs. Since the carbon coating greatly increases the electrochemical performance of the composite electrode,<sup>20</sup> it is of interest to evaluate the thickness of the coating in more detail. The SAXS profile of C- $\text{TiO}_2$  shows an enhancement at  $q = \sim 0.5$   $\text{nm}^{-1}$  and gives evidence of larger nanostructures in the sample. This could be due to aggregate formation as also proposed in previous works.<sup>20,19,27</sup> We report also in Figure S4 a representative TEM image of the C- $\text{TiO}_2$  sample. The log-normal size distribution of the C- $\text{TiO}_2$  NPs was found by fitting with a core–shell model and is shown in Figure 2b. The parameters extracted from the fits are presented in Table 1. The log-normal size distribution is weighted by the nanoparticle volume, which gives information about the actual volume distribution of the NPs.<sup>28</sup> The diameter determined via SAXS,  $D_{\text{SAXS}}$ , and its standard deviation,  $\sigma$ , confirm the expected size ( $\sim 15$  nm) for the commercial  $\text{TiO}_2$  material while demonstrating a smaller size for the synthesized C- $\text{TiO}_2$  NPs ( $\sim 8$  nm). The aggregate contribution does not affect the size distribution of the nanoparticles but could affect the evaluation of the shell. The carbon coating on the  $\text{TiO}_2$  should be evaluated further to understand the morphological implications.

From SAXS, TEM,<sup>18</sup> and XRD we can assume that the C- $\text{TiO}_2$  NPs have a mean diameter of  $\approx 8$  nm with a quasispherical shape and that the main anatase atomic structure is not affected by the carbon coating.<sup>20</sup> Due to the dimensions of the  $\text{TiO}_2$  NPs under study, we can consider the local structure to be very similar to the bulk crystalline material, as shown in previous theoretical works.<sup>21,20,29,30</sup> EXAFS data were evaluated by using theoretical calculations of the absorption cross-section obtained by the GNXAS method.<sup>24,25</sup> This allows the theoretical EXAFS signal to be obtained for various two-body and three-body configurations of the typical anatase structure in a cluster of about  $\approx 6$  Å,<sup>24,25</sup> as presented in Figure 1.

**C- $\text{TiO}_2$  Nanoparticles: Local Structure.** EXAFS spectra of the Ti  $K$ -edge can be used to probe the local structure of the C- $\text{TiO}_2$  anatase NPs. Herein, the X-ray absorption near-edge (XANES) region of the spectra is evaluated qualitatively, while

**Table 1.** Cell Parameters Obtained by Rietveld Refinement of the XRD Scans ( $a$  and  $c$ , nm), Crystallite Size Obtained from the Debye–Scherrer Equation ( $D_{\text{XRD}}$ ), Volume-Weighted Diameter Obtained by SAXS Fitting ( $D_{\text{SAXS}}$ ), and Standard Deviation Calculated from the Lognormal Size Distribution in Figure 2b ( $\sigma_{\text{SAXS}}$ )

sample	$a$ (nm)	$c$ (nm)	$D_{\text{XRD}}$ (nm)	$D_{\text{SAXS}}$ (nm)	$\sigma_{\text{SAXS}}$ (nm)
TiO <sub>2</sub>	0.379 28(3)	0.952 70(9)	19(2)	15	2
C-TiO <sub>2</sub>	0.379 23(5)	0.9522(1)	9(2)	8	3

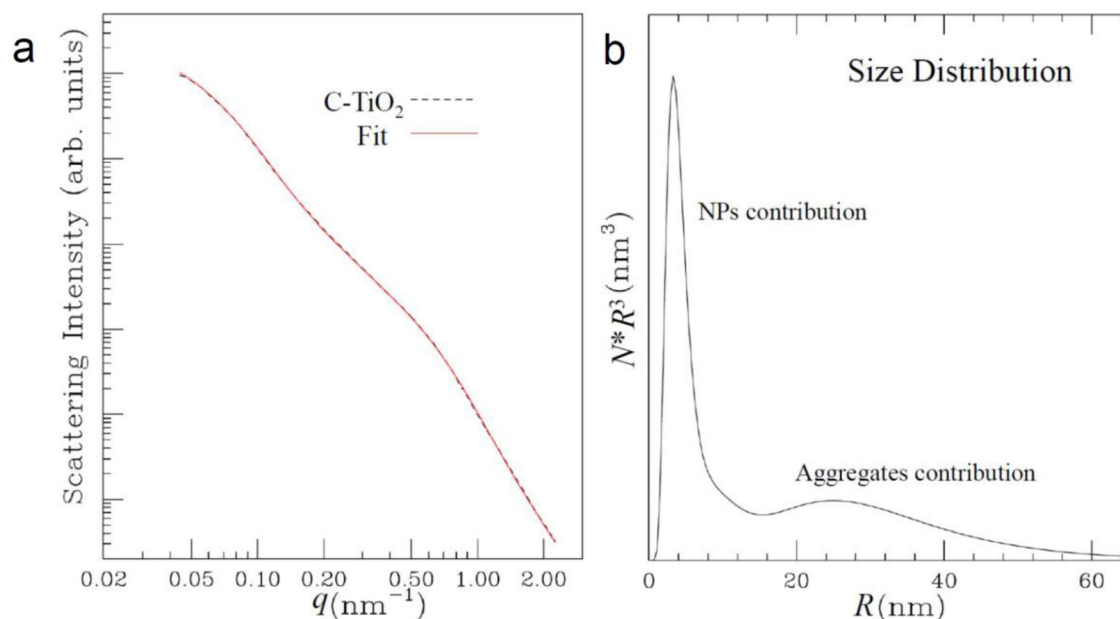


**Figure 2.** (a) Best fit of the SAXS profile of the C-TiO<sub>2</sub> NPs. (b) Log-normal size distribution obtained by fitting the C-TiO<sub>2</sub> nanoparticle SAXS profile with a core–shell model and aggregates contribution.<sup>27</sup> The volume-weighted size distribution refers to the core particles only.

the EXAFS region is analyzed more extensively according to multiple scattering (MS) theory. All results for the synthesized C-TiO<sub>2</sub> NPs are compared to the commercially available TiO<sub>2</sub> NPs from Sigma-Aldrich. Figure 3 displays the XANES spectra of C-TiO<sub>2</sub>, which show the typical features of the anatase

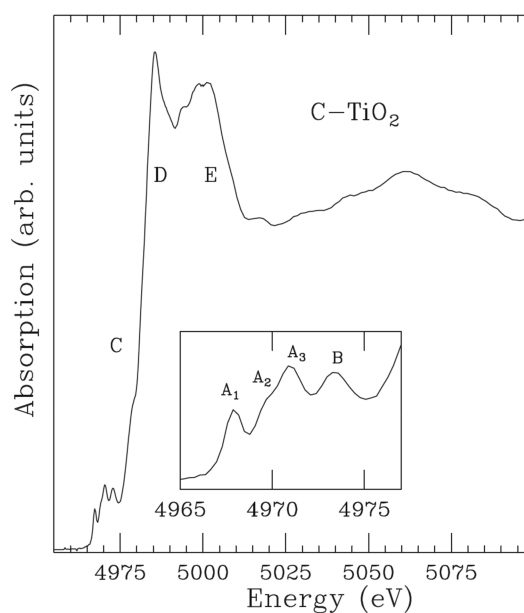


**Figure 3.** XANES region of the C-TiO<sub>2</sub> nanoparticles at the Ti K-edge; the inset shows the pre-edge features.

structure consisting of 4 prepeak features labeled A<sub>1</sub>, A<sub>2</sub>, A<sub>3</sub>, and B, a shoulder labeled as C, and two main peaks, D and E, after the edge.<sup>29,31,32</sup> Figure S5 of the Supporting Information compares the Ti K-edge XANES spectra of C-TiO<sub>2</sub> NP and TiO<sub>2</sub> NP powders and the composite pristine electrode, S<sub>0</sub>, with that of Ti metal. The K-edge position of the Ti metal is found at 4965.0 eV while the C-TiO<sub>2</sub> sample shows a chemical shift of 17.2 eV from that of Ti metal. No differences among the powders and the pristine electrode, S<sub>0</sub>, are present.

The main electronic transition, the so-called white line (peak D), arises from the dipole selection rule ( $\Delta l = +1$ ) and is the  $1s \rightarrow 4p$  transition, but the 3d transition metals and their oxides have a partially filled 3d band,<sup>33</sup> giving rise to additional and less probable transitions. To explain the pre-edge features, Wu et al.<sup>29</sup> proposed the molecular orbital (MO) energy-level diagram for the octahedral coordinated (TiO<sub>6</sub>)<sup>8-</sup> molecule shown in Figure S6. Looking at the MO diagram in Figure S6 and Figure 3, the peak A<sub>1</sub> is assigned to  $1s \rightarrow t_{1g}$  transition, while A<sub>2</sub> and A<sub>3</sub> are attributed to  $1s \rightarrow 3d$  designated as the  $1s \rightarrow 2t_{2g}$  and  $1s \rightarrow 3e_g$  transitions, respectively.<sup>34</sup> Peak B is different, as it is dipolar in nature and related to medium range order through the hybridization of the central Ti 4p orbital with the second shell Ti 3d orbitals and is assigned to the  $4p \rightarrow 4s$  transition.<sup>31,33,35</sup>

In Figure 1a the primitive cell of TiO<sub>2</sub> anatase is shown. From this figure it is possible to visualize the octahedron formed by one titanium atom and six oxygen atoms, where four of the oxygen atoms have a distance of 1.94 Å, and two have a distance of 1.99 Å from Ti. The elongation of the interatomic distance of the azimuthal oxygen atoms is known as Jahn–

Teller distortion.<sup>36</sup> The signals arising in  $A_2$  and  $A_3$  mirror a different degree of hybridization due to Jahn–Teller distortion<sup>37</sup> on the  $(\text{TiO}_6)^{8-}$  octahedral molecule. This means that, due to the two different distances between the central Ti 4p orbitals of the two Ti shells (see the inset of Figure S6), two signals are generated.

A simulated cluster of anatase  $\text{TiO}_2$  about  $\approx 6$  Å in diameter is shown in Figure 1b. Taking the bulk  $\text{TiO}_2$  anatase and the primitive cell shown in Figure 1a, in Tables 2 and 3 and in

**Table 2. Two-Body ( $g_2$ ) Configurations in a Typical Anatase Structure (Labeled as theo) for the Ti K-Edge Compared to Those Extracted from a Best Fit (Labeled as exp)<sup>a</sup>**

atoms	shell	$R_{\text{theo}}$ (Å)	$N_{\text{theo}}$	$R_{\text{exp}}$ (Å)	$\sigma^2$ (Å <sup>2</sup> )	$N_{\text{exp}}$
Ti–O	I	1.945	4	1.945	0.008	4
Ti–O	I	1.995	2	1.995	0.005	2
Ti–O	X-phase			2.520	0.021	6
Ti–Ti	II	3.065	4	3.065a <sup>b</sup>	0.009a <sup>b</sup>	4
Ti–Ti	III	3.804	4	3.804b <sup>b</sup>	0.039b <sup>b</sup>	4
Ti–O	IV	3.890	8	3.899	0.006	8

<sup>a</sup> $R_M$  ( $M = \text{theo or exp}$ ) is the mean distance between atoms Ti–A ( $A = \text{O or Ti}$ ).  $N_M$  ( $M = \text{theo or exp}$ ) is the coordination number, and  $\sigma^2$  is the Debye–Waller parameter up to the IV shell, obtained from the best fit. The II and III shell parameters are obtained from the three-body configurations in Table 3. <sup>b</sup>Derived from three-atom configurations with the same label in Table 3.

**Table 3. (Upper Panel, Theoretical) Three-Body ( $g_3$ ) Configurations in a Typical Anatase Structure for the Ti K-edge;<sup>a</sup> (Lower Panel, Experimental): Same Parameters but Extracted from the Best Fit Analysis**

atoms	$R_1$ (Å)	$R_2$ (Å)	angle (deg)	deg.
Theoretical				
O–Ti–Ti	1.945	1.995	102.10	4
O–Ti–Ti	1.945	1.945	155.81	4
Ti–O–O	1.995	1.995	180.00	1
Experimental				
O–Ti–Ti <sup>a</sup>	1.945	1.995	102.10	4
O–Ti–Ti <sup>b</sup>	1.945	1.945	155.80	4
Ti–O–O	1.995	1.995	180.00	1

<sup>a</sup> $R_1$  and  $R_2$  are the mean distances of two shortest bonds with angle in between. deg. is the degeneracy for each configuration, with the first atom placed at the vertex between the two shortest bonds (e.g., Ti–O–O: Ti atom is at the vertex), but the photoabsorber is always Ti.

Figure 1b, the expected atomic configurations in the limit of the EXAFS technique within 5–6 Å are shown. The details of the EXAFS theory and model can be found in the previously reported literature.<sup>24</sup>

Our modeling of the local structure includes the following two- and three-body contributions (see also Figure 1a). The two-body signals,  $g_2$ , for Ti–O and Ti–Ti were modeled as Gaussian distributions with three parameters: the average distance between atoms,  $R$ , the variance,  $\sigma^2$  (Debye–Waller parameter), and the coordination number,  $N_c$ . We accounted for both two-body and three-body signals using O–Ti–Ti and Ti–O–O triangular configurations formed by the two nearest-neighbor bonds, with bond angles of 102°, 155°, and 180° (see Figure 4). The  $N_c$  and degeneracy of the triangular configurations were fixed according to the theoretical structure (Tables 2 and 3). We used diagonal covariance matrices for the thermal average, thereby introducing the bond-angle-variance,

$\sigma^2$ , as an additional parameter.<sup>24,25</sup> Only the signals and three-body configurations that give rise to stronger contributions were considered.<sup>20,21</sup>

In Figure 4, the MS best fit of the C–TiO<sub>2</sub> NPs is shown. A comparison between the theoretical (labeled as theo) and experimental (labeled as exp) structural parameters are presented in Tables 2 and 3. The presence of an additional Ti–O signal at  $\approx 2.5$  Å leads us to conclude that an additional phase (X-phase) is present that was not previously revealed by XRD and whose content must be less than 5% by weight. To prove the presence of this additional phase, the MS best fit and Fourier transform (FT) without inclusion of the X-phase contribution were analyzed, as can be seen in Figure S7 of the Supporting Information. Without this additional X-phase contribution, it is not possible to fit the EXAFS signal properly. In particular, this 2.5 Å interatomic distance two-body signal can be assigned to an orthorhombic TiO<sub>2</sub>  $Pnma$  phase<sup>38</sup> that most likely arises from the synthetic procedure. The same two body signal was found in the TiO<sub>2</sub> NPs from Sigma-Aldrich. This distance was determined via the MS best fit and is reported in Table 2.

The parameters defining the first-shell distributions (i.e.,  $R$  and  $\sigma^2$  for I shell in Tables 2 and 3) are those measured with higher accuracy, as they are related both to the direct nearest-neighbor two-body signal and to several MS contributions. The best fit nearest-neighbor structural results are in good agreement with those of a previous analysis.<sup>32,39</sup> In light of these results, we can now apply the fitting procedure to the electrodes to follow the structural modifications induced by the sodiation effect.

#### C-TiO<sub>2</sub> Composite Electrodes: The Sodiation Effect.

The typical voltage profile of a C–TiO<sub>2</sub> composite electrode upon sodiation is shown in Figure S1. In this cell, employing Na metal as the counter electrode, the C–TiO<sub>2</sub>-based electrode acts as the positive (cathode) electrode. During the first step, the C–TiO<sub>2</sub> material is sodiated (i.e., sodium is inserted), leading to the reduction of TiO<sub>2</sub>. At the end of the step, the electrode potential is only 20 mV above that of Na metal plating; thus, the C–TiO<sub>2</sub> material can be considered as fully sodiated. Upon the subsequent step, Na<sup>+</sup> ions and the corresponding electrons are removed from the C–TiO<sub>2</sub> electrode resulting in the oxidation of the active material. As seen in Figure S1, the process is rather irreversible; i.e., the amount of charge needed to achieve full sodiation of the material is much larger than the charge needed to fully desodiate it. This irreversibility, frequently observed in TiO<sub>2</sub> anatase materials upon lithiation and sodiation,<sup>40</sup> is associated with the formation of the solid electrolyte interphase (SEI) resulting from the reductive decomposition of electrolyte components, which inhibits further reaction between the sodiated electrode and the electrolyte. However, an irreversible transformation of the active material itself (TiO<sub>2</sub>) cannot be excluded.<sup>21,41–47</sup> The occurrence of reversible and irreversible transformations in the electronic and crystalline structure of the active material is investigated in the following paragraphs.

Figure S5 compares the EXAFS spectra of a pristine composite C–TiO<sub>2</sub> electrode,  $S_0$ , and the neat C–TiO<sub>2</sub> powder, showing no substantial differences. From this result along with the XRD results, which shows no differences after electrode preparation, it can be concluded that the electrode preparation procedure does not influence the crystalline or electronic structures of the active material.

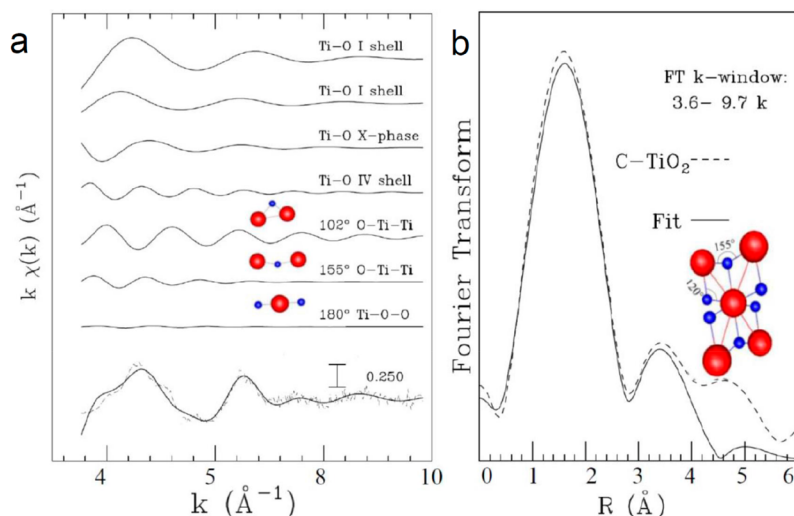


**Figure 4.** (a) Best fit of C-TiO<sub>2</sub> NPs EXAFS (dashed line). The scale 0.250 Å<sup>-1</sup> is inside the figure. In the inset, the three body contributions used in the fit are represented. The theoretical signals (solid line) are shifted for clarity. (b) FT of the theoretical (solid line) and the experimental (dashed line) EXAFS signal. The parameter values extracted from the fits are presented in Tables 2 and 3. In the inset of the FT window is the ball and stick model of the three body configurations used for the fit. For the ball and stick models the red spheres represent Ti atoms, and the blue spheres correspond to O atoms.

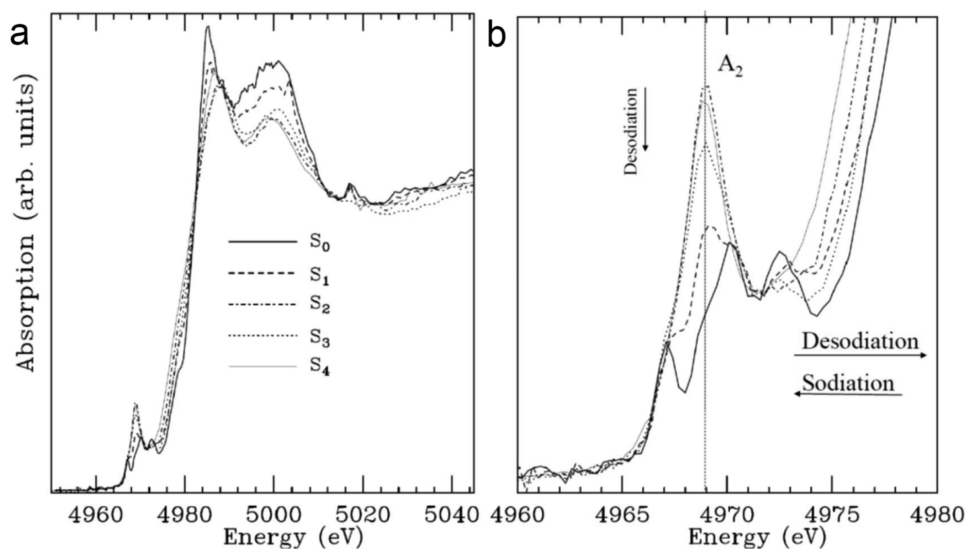


**Figure 5.** (a) Ti *K*-edge spectra in the XANES region for electrodes at different states of charging, and (b) magnification of the pre-edge features. The arrows show the trend of the spectra due to the 1st sodiation and the 1st and 2nd desodiation.

Figure 5a shows the normalized XANES spectra along with a zoomed in region highlighting the pre-edge features in Figure 5b. It has been demonstrated that the pre-edge features of the Ti *K*-edge spectra reflect the octahedral geometry, while an increase in the intensity of the A<sub>2</sub> peak is due to distortions and defects in the Ti atom site as it becomes more non-centrosymmetric relative to perfect TiO<sub>2</sub>.<sup>48</sup> As can be seen in the XANES spectra in Figure 5a,b, it is evident that the A<sub>2</sub> peak increases upon cycling, in particular after the first sodiation. During desodiation, and in particular for the fully desodiated sample at 2.00 V (S<sub>3</sub>), a decrease in the A<sub>2</sub> pre-edge feature can be observed.

It is also possible to observe a shift in the edge position upon cycling in Figure 5a, which will occur upon a change in the oxidation state between 4<sup>+</sup> and 3<sup>+</sup>. The determined edge

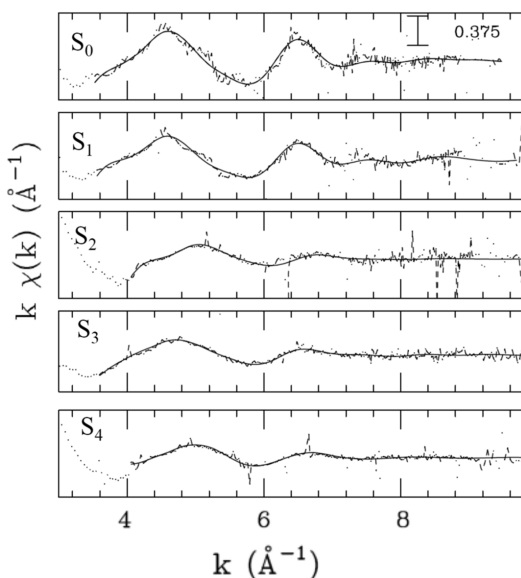
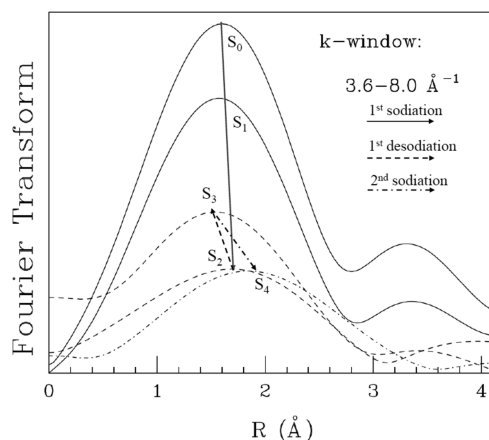
positions and the relative valence states are in good agreement with the electrochemical behavior, as presented in Table 4.

To correlate the pre-edge features with the structural changes upon cycling, a detailed EXAFS analysis is reported. In particular, Figures 6 and 7 show the EXAFS signals of the electrodes along with their Fourier transforms, while Table 5 presents the main results up to the III shell as obtained by a best fit analysis. The SRO of the pristine electrode shows the identical and well-defined anatase structure of the C-TiO<sub>2</sub> pristine material. With the onset of sodiation, in sample S<sub>1</sub>, the pre-edge features immediately start changing alongside the atomic structure. This includes an almost complete disappearance of Jahn–Teller distortion, where *R*<sub>1</sub> and *R*<sub>2</sub> develop similar values. In addition, there is an increase in the Debye–Waller parameter, in particular for the Ti–Ti II shell signal (Table 5, σ<sub>3</sub><sup>2</sup>); these changes are related to the atomic

**Table 4.** Ti K-Edge Position and the Relative Estimated Valence State Related to the Electrochemical Results

sample	edge (eV)	valence by XAS	valence by electrochemistry
Ti metal	4965.0	0	
TiO <sub>2</sub> NP	4983.0	4.00	
C-TiO <sub>2</sub>	4983.0	4.00	
S <sub>0</sub>	4983.0	4.00	
S <sub>1</sub>	4982.6	3.91	N/A <sup>a</sup>
S <sub>2</sub>	4982.7	3.97	3.9
S <sub>3</sub>	4982.2	3.80	3.8
S <sub>4</sub>	4978.2	3.00	3.0

<sup>a</sup>For sample S<sub>1</sub> it is not possible to distinguish the SEI formation from the active material reduction.

**Figure 6.** Extracted EXAFS signal for the electrodes at different states of charging; the scale 0.375 Å<sup>-1</sup> is indicated inside the picture.**Figure 7.** Fourier transform of the EXAFS signals shown in Figure 6 for the different electrodes; arrows are only a guide for the reader and are related to the different sodiation cycles. Solid line for the 1st sodiation, dashed for the 1st desodiation, and dash-dotted line for the 2nd sodiation, where the degrees of sodiation are shown in Figure S1.

structural modification and disorder. The I shell coordination number,  $N_{cl}$ , for the Ti–O signal decreases, revealing the

coexistence of 6- and 5-fold coordination, which indicates that a loss of oxygen has begun at this stage. However, the LRO still largely maintains contributions from the anatase structure, as made evident in the XRD profile in Figure S8 for sample S<sub>1</sub>.

After the first complete sodiation and first desodiation to 0.4 V (sample S<sub>2</sub>), the LRO of the atomic structure appears to already be mostly disordered, where the XRD scans in Figure S8 show no discernible signals. At the SRO, the EXAFS signals and their Fourier transforms (FTs), as shown in Figures 6 and 7, respectively, show a substantial decrease in intensity and a shift toward higher values. The Debye–Waller parameter largely increases for all signal contributions, and the first shell coordination number,  $N_{cl}$ , also changes toward a 5-fold coordination, as shown in Table 5. The Jahn–Teller distortion disappears along with a significant increase in the pre-edge A<sub>2</sub> feature (Figure 5b). The lack of 6-fold coordination indicates that the oxygen loss is already complete at this stage.

At the fully desodiated state at 2.00 V (sample S<sub>3</sub>), the reversibly stored sodium is completely removed, resulting in the partial reordering of the SRO as made evident in the FT in Figure 7, where the intensity is increased, and the relative Debye–Waller parameter,  $\sigma_1^2$ , is decreased. Moreover, there is a reappearance of Jahn–Teller distortion as reported in Table 5, with a decrease in  $R_1$  in addition to a simultaneous shift in the FT toward lower values, as can be seen in Figure 7. The pre-edge feature, A<sub>2</sub>, is also observed to decrease as a fingerprint of the local partial reordering of the structure. However, according to XRD in Figure S8, no evidence of a partial reordering of the LRO can be observed.

When the electrode is sodiated for the second time (sample S<sub>4</sub>), the reversible cycle is completed. No II shell and III shell contributions remain, and only the 5-fold I shell Ti–O signal at a distance of 2.00 Å is observed. Again, bonding elongation and structural disorder occur that are also evident in the FT and EXAFS signals (Figures 6 and 7, respectively) along with an increase in the intensity of the pre-edge feature, A<sub>2</sub>. At the same time, the main peaks labeled as D and E of the main transition 1s → 4p in the XANES region decrease together with the rearrangement of the atomic structure, where only a slight increase in the D peak for the fully sodiated sample is observed. The D peak also shows a slight and continuous shift toward higher energy values for all electrodes except again for the fully sodiated sample, S<sub>4</sub>, which is most similar to S<sub>1</sub>, as can be seen in Figure 5a. The observed intensity changes in the white line are inversely proportional to the electronic population of the final state, 4p, where the intensity decrease of the white line reflects a more populated final electronic state, 4p, and *vice versa*.

Upon cycling, the X-phase does not show any particular changes, which seems to imply that it does not play an active role in the sodiation–desodiation process.

A schematic summary of the structural behavior is presented in Figure 8 alongside the observed changes in the pre-edge features. The pre-edge features were further analyzed by subtracting the contribution of the main 1s → 4p transition. In Figure 8 the intensity of B was kept constant. In fact, due to the different nature of peak B, it can be used for comparison with the other peaks because it is independent of the hybridization state of the Ti 3p atom.<sup>35</sup> Figure S9 shows the possible 5-fold coordination configurations represented by trigonal bipyramidal and square pyramidal structures. Due to the initial octahedral structure, we consider it to be more likely that the structure rearranges to trigonal bipyramidal. The

Table 5. Best Fit Parameters up to the III Shell (sh) for Different States of Charging<sup>a</sup>

sample	Ti–O			I sh			Ti–O			I sh			Ti–Ti			II sh			Ti–Ti			III sh				
	$R_1$ (Å)	$\sigma_1^2$ (Å <sup>2</sup> )	$N_{c1}$	$R_2$ (Å)	$\sigma_2^2$ (Å <sup>2</sup> )	$N_{c2}$	$R_x$ (Å)	$\sigma_x^2$ (Å <sup>2</sup> )	$N_{cx}$	$R_3$ (Å)	$\sigma_3^2$ (Å <sup>2</sup> )	$N_{c3}$	$R_4$ (Å)	$\sigma_4^2$ (Å <sup>2</sup> )	$N_{c4}$	$R_5$ (Å)	$\sigma_5^2$ (Å <sup>2</sup> )	$N_{c5}$	$R_6$ (Å)	$\sigma_6^2$ (Å <sup>2</sup> )	$N_{c6}$	$R_7$ (Å)	$\sigma_7^2$ (Å <sup>2</sup> )	$N_{c7}$		
S <sub>0</sub>	1.945	0.008	4.0	1.995	0.005	2.0	2.520	0.021	6.0	3.065	0.009	4.0	3.899	0.066	4.0											
S <sub>1</sub>	1.971	0.009	3.7	1.974	0.009	1.8	2.538	0.024	6.0	3.078	0.083	3.8	3.880	0.065	3.8											
S <sub>2</sub>	1.970	0.025	5.0				2.540	0.034	6.0	3.102	0.031	3.3	3.819	0.063	3.3											
S <sub>3</sub>	1.920	0.007	1.7	2.031	0.032	3.3	2.495	0.039	6.0	3.041	0.028	3.3	3.857	0.004	3.3											
S <sub>4</sub>	2.009	0.028	5.0				2.560	0.027	6.0																	

<sup>a</sup> $R_n$  is in Å, and represents the interatomic distance between the 2-body species related to the shell.  $\sigma_n^2$  is in Å<sup>2</sup> and is the Debye–Waller parameter related to  $R_n$ .  $N_{cn}$  is the related coordination number. In all cases,  $n$  corresponds to the shell number.

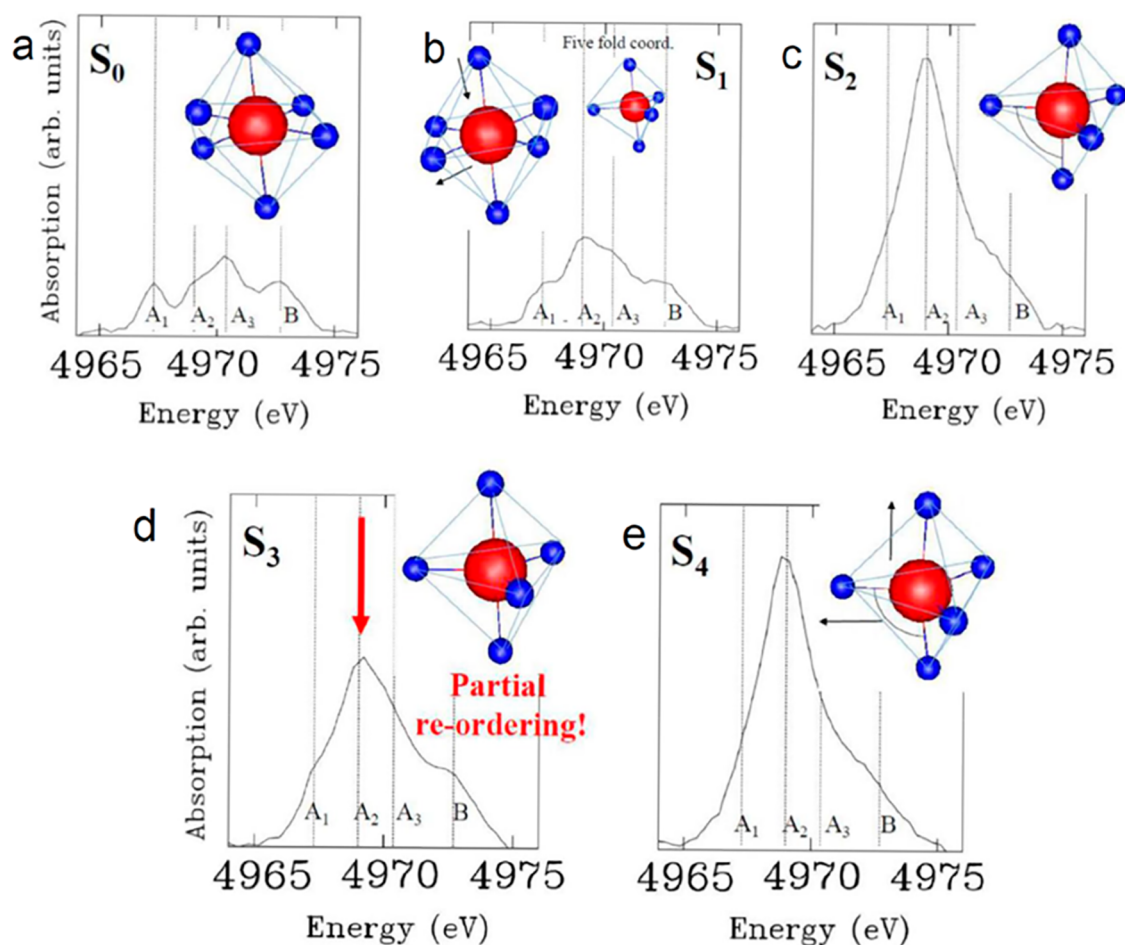


**Figure 8.** Normalized pre-edge features of the Ti K-edge for the electrodes at different states of charging: (a) pristine, (b) sodiated at 0.30 V, (c) desodiated at 0.40 V, (d) fully desodiated at 2.00 V, and (e) fully sodiated at 0.02 V. The insets show the most probable 6- and 5-fold configurations for the Ti–O bonds as related to the obtained EXAFS fitting parameters. In part b there is the coexistence of 5- and 6-fold configurations, with the major contribution arising from the 6-fold configuration. The arrow in panel d serves to highlight the decrease of the intensity of peak A<sub>2</sub> due to electrochemically induced partial reordering.

proposed Ti–O configurations in the insets of Figure 8 are obtained by the EXAFS results, also for the three-body angles included in the fit that are shown in Figure 4.

## CONCLUSIONS

The structural modifications induced by electrochemical Na<sup>+</sup> insertion in carbon-coated TiO<sub>2</sub> NPs were investigated in this work by means of XRD and XAS, giving a full investigation in terms of LRO, SRO, and electronic structure. Overall, the TiO<sub>2</sub> anatase structure undergoes substantial rearrangement upon sodiation. The process is rather irreversible during the first

sodiation, mostly due to the formation of the SEI, but also involving the overall amorphization of the TiO<sub>2</sub> structure in the final sodiation stage. Oxygen loss occurs, as confirmed by the transition from 6-fold to 5-fold coordination between Ti and O according to the EXAFS results and also by the decrease of the white line in the XANES spectra, which is in agreement with electrochemical oxygen loss observed in our earlier work.<sup>19</sup> However, no trace of metallic Ti is found via XAS analysis, leading to the conclusion that its presence in previous work,<sup>19</sup> as detected by XPS, was actually an artifact due to the sputtering process.

Gas generation upon electrochemical cycling is a serious problem for electrode materials because it can result in catastrophic failure of the cells. The release of oxygen is even more dangerous since it contributes to the possibility of fire in the cell. However, the oxygen loss appears to occur only upon the first cycle, i.e., upon cell formation, when the SEI growth is also generating various gases, which are (or can easily be) removed before the cell is released for use. Thus, the carbon-coated TiO<sub>2</sub> NPs can be safely used as an anode material for Na-ion batteries.

Finally, a partial, short-range electrochemically induced ordering is observed upon recharge, but as a result of the oxygen loss, in the trigonal bipyramidal structure rather than the original orthorhombic one. The obtained results lead us to conclude that the robust approach for nano and amorphous material characterization can also be applied during operando investigations and with other nanocrystalline functional systems.

## ■ EXPERIMENTAL METHODS

**Sample Preparation.** Electrodes were prepared using C-TiO<sub>2</sub> materials according to previously reported procedures.<sup>20</sup> The dry C-TiO<sub>2</sub> electrodes had a composition of 65 wt % TiO<sub>2</sub>, 25 wt % carbon [accounting for the carbon present in the C-TiO<sub>2</sub> particles and the conductive agent (Super C65, IMERYS, Switzerland)], and 10 wt % binder (polyvinylidene fluoride PVDF, ARKEMA), while the uncoated TiO<sub>2</sub> electrode composition was 65 wt % TiO<sub>2</sub>, 25 wt % Super C65, and 10 wt % PVDF. Three-electrode cells were assembled in a drybox (H<sub>2</sub>O and O<sub>2</sub> content lower than 1 ppm) using the prepared electrodes as the working electrodes. The electrolyte was a 1 M solution of NaClO<sub>4</sub> (98% Sigma-Aldrich) dissolved in a 1:1 mixture (by volume) of ethylene carbonate (UBE) and propylene carbonate (Sigma-Aldrich). Sodium metal (99.8%, ACROS ORGANICS) was used as both the counter and reference electrodes. Thus, all given potentials in this paper refer to the Na/Na<sup>+</sup> reference couple. Sodiation at each desired level was achieved by applying a constant current to the three-electrode cells to a predefined electrode potential; this potential was then held for at least 1 h to allow equilibration of the electrode bulk. After sodiation to the desired level, the cells were disassembled, and the electrodes were carefully rinsed in dimethyl carbonate (DMC Sigma-Aldrich 99.9%, anhydrous) to remove any residual electrolyte. The sample preparation and cell assembly and disassembly were performed in an Ar-filled glovebox (with oxygen and water concentrations lower than 0.1 ppm) to avoid any reactions with oxygen or moisture. The transfer from the glovebox to the instruments was done using an airtight container.

**X-ray Diffraction (XRD).** XRD measurements for the TiO<sub>2</sub> NPs from Sigma-Aldrich and the pristine C-TiO<sub>2</sub> powders were performed on a Bruker D8 Advance diffractometer using Cu K $\alpha$  radiation at Helmholtz Institute Ulm (HIU) laboratories.

XRD measurements for the composite electrodes were performed under Ar atmosphere in an inert gas holder. The diffraction scans were collected at the Energy Materials In-Situ Laboratory Berlin (EMIL), jointly operated by Helmholtz-Zentrum Berlin für Materialien und Energie, GmbH (HZB) and the Max-Planck Society (MPG), on a Bruker D8 diffractometer using Cu K $\alpha$  radiation ( $\lambda_{\text{CuK}\alpha} = 1.54187 \text{ \AA}$ ) in grazing-incidence geometry.

All scans were recorded over  $2\theta = 20\text{--}100^\circ$ . For all grazing incidence measurements, a step size of  $0.02^\circ$  and a  $3^\circ$  incident angle ( $\theta$ ) were used, along with a  $2.5^\circ$  primary soller slit to define the beam. Rietveld refinement was performed using the Maud program.<sup>34</sup>

**Small-Angle X-ray Scattering (SAXS) and X-ray Absorption Spectroscopy (XAS).** SAXS and XAS were carried out at the synchrotron radiation beamline FCM (Four Crystal Monochromator) of the Physikalisch-Technische Bundesanstalt (PTB) at BESSY II, operated by Helmholtz-Zentrum Berlin.<sup>49</sup> The incoming photon flux was monitored by a  $7 \mu\text{m}$  thick silicon photodiode.<sup>50</sup> The sample transmission was also measured by a silicon photodiode.

SAXS measurements were performed with an in-vacuum PILATUS 1 M hybrid-pixel detector on the pure and carbon-coated TiO<sub>2</sub> powders after being fixed on Kapton tape. Each image was collected for 500 s at 4944 eV at two sample to detector distances to obtain a momentum transfer range of  $0.03 \text{ nm}^{-1} < q < 2.00 \text{ nm}^{-1}$ . The obtained SAXS images were integrated to obtain the scattering intensity as a function of the momentum transfer. The measured transmittance of the sample and the Kapton tape was taken into account. The fitting was carried out with the SASfit code,<sup>51</sup> and log-normal particle size distributions were assumed. From the fit results, the volume-weighted diameter and the standard deviation of the size distribution were extracted.

All XAS measurements were performed in transmission mode at the Ti K-edge (4965 eV), where both TiO<sub>2</sub> powder samples as well as the TiO<sub>2</sub> composite electrodes were examined. For the powder samples, pellets were prepared by carefully mixing the TiO<sub>2</sub> powders with graphite, to produce samples with appropriate thickness to give an optimal jump ratio at the Ti K absorption edge of about 1.2.<sup>23</sup> The TiO<sub>2</sub> composite electrodes were examined as extracted from the cells, i.e., in the form of a composite layer coated on a copper current collector prepared as described above.

The background in the XANES region was fitted by a straight line between 4945 and 4957 eV and subsequently subtracted from all spectra. For the pre-edge evaluation, the main  $1s \rightarrow 4p$  transition was subtracted with the Fityk program.<sup>52</sup>

**EXAFS Theoretical Method.** The GNXAS method is based on multiple scattering (MS) evaluation and has previously been successfully applied to various nanocrystalline systems such as nanocatalysts for fuel cells.<sup>22,23</sup> The Ti K-edge EXAFS experimental data of the resulting TiO<sub>2</sub> configurations were subsequently analyzed using the MS contributions through  $n$ -body  $\gamma$  signals. The total  $\gamma$  signal is the sum of the two-body and three-body  $\gamma$  signals ( $\gamma_{(2)}$  and  $\gamma_{(3)}$ ) associated with contributions from the pair and triplet atomic configurations (hereafter called  $g_2$  and  $g_3$  peaks) as described in detail in the GNXAS manual and in the literature.<sup>24,25</sup> These contributions were used for *ab initio* calculations from the theoretical model of the anatase hexagonal structure using nonoverlapping potentials within the muffin-tin approximation ( $RT_{\text{MT}} = 0.97 \text{ \AA}$  for a first-neighbors distance  $R_{\text{FN}} \approx 1.94 \text{ \AA}$ ). The inelastic mean-free path (MFP) of the excited photoelectron used for the energy dependent Hedin–Lundqvist potential has been automatically calculated, while its core-hole lifetime is a constant parameter taken from Krause, et al.<sup>53</sup>

At room temperature, the electron mean free path and the atomic vibrations are limited to a sphere of about 6 Å from the photoabsorbing atom. As a result, the main frequency contributions of the  $\chi(k)$  signal are calculated within this range. Moreover, the conventional disorder has been taken into account by using both signals arising from  $g_2$  and  $g_3$  as a Gaussian function, and averaging the signals  $g_2$  and  $g_3$ .<sup>24,25</sup>

## ■ ASSOCIATED CONTENT

### § Supporting Information

The Supporting Information is available free of charge on the ACS Publications website at DOI: 10.1021/acsam.9b01101.

Sodium-ion battery voltage profile, XRD profiles, SAXS profile, FT, XANES spectra, molecular-orbital energy-level diagram, EXAFS fitting, and a schematic of Ti and O coordination configurations (PDF)

## ■ AUTHOR INFORMATION

### Corresponding Authors

\*E-mail: giorgia.greco@helmholtz-berlin.de.

\*E-mail: stefano.passerini@kit.edu.

### ORCID

Giorgia Greco: 0000-0002-4612-5840

Katherine A. Mazzio: 0000-0001-9565-7301

Robert Wendt: 0000-0001-8480-4775

Stefano Passerini: 0000-0002-6606-5304

## Notes

The authors declare no competing financial interest.

## ACKNOWLEDGMENTS

S.P. and X.D. would like to acknowledge the basic support of the Helmholtz Association. Dr. M. N. Tahir and Prof. W. Tremel (Institute of Inorganic & Analytical Chemistry, Johannes Gutenberg University, Mainz, Germany) are kindly acknowledged for the supply of the C-TiO<sub>2</sub> material. X.D. acknowledges the fellowship of the Chinese Scholarship Council. G.G. would like to thank also L. Fumagalli, A. Hoell, K. Effland, and L. Cibik.

## REFERENCES

- (1) Larcher, D.; Tarascon, J.-M. Towards Greener and More Sustainable Batteries for Electrical Energy Storage. *Nat. Chem.* **2015**, *7* (1), 19–29.
- (2) Hwang, J.-Y.; Myung, S.-T.; Sun, Y.-K. Sodium-Ion Batteries: Present and Future. *Chem. Soc. Rev.* **2017**, *46* (12), 3529–3614.
- (3) Eftekhari, A.; Kim, D.-W. Sodium-Ion Batteries: New Opportunities beyond Energy Storage by Lithium. *J. Power Sources* **2018**, *395*, 336–348.
- (4) Vaalma, C.; Buchholz, D.; Weil, M.; Passerini, S. A Cost and Resource Analysis of Sodium-Ion Batteries. *Nat. Rev. Mater.* **2018**, *3* (4), 18013.
- (5) Hasa, I.; Hassoun, J.; Passerini, S. Nanostructured Na-Ion and Li-Ion Anodes for Battery Application: A Comparative Overview. *Nano Res.* **2017**, *10* (12), 3942–3969.
- (6) Kubota, K.; Dahbi, M.; Hosaka, T.; Kumakura, S.; Komaba, S. Towards K-Ion and Na-Ion Batteries as “Beyond Li-Ion”. *Chem. Rec.* **2018**, *18* (4), 459–479.
- (7) Deng, J.; Luo, W.-B.; Chou, S.-L.; Liu, H.-K.; Dou, S.-X. Sodium-Ion Batteries: From Academic Research to Practical Commercialization. *Adv. Energy Mater.* **2018**, *8* (4), 1701428.
- (8) Pu, X.; Wang, H.; Zhao, D.; Yang, H.; Ai, X.; Cao, S.; Chen, Z.; Cao, Y. Recent Progress in Rechargeable Sodium-Ion Batteries: Toward High-Power Applications. *Small* **2019**, *15*, 1805427.
- (9) Roberts, S.; Kendrick, E. The Re-Emergence of Sodium Ion Batteries: Testing, Processing, and Manufacturability. *Nanotechnol., Sci. Appl.* **2018**, *11*, 23–33.
- (10) Bauer, A.; Song, J.; Vail, S.; Pan, W.; Barker, J.; Lu, Y. The Scale-up and Commercialization of Nonaqueous Na-Ion Battery Technologies. *Adv. Energy Mater.* **2018**, *8* (17), 1702869.
- (11) Hasa, I.; Dou, X.; Buchholz, D.; Shao-Horn, Y.; Hassoun, J.; Passerini, S.; Scrosati, B. A Sodium-Ion Battery Exploiting Layered Oxide Cathode, Graphite Anode and Glyme-Based Electrolyte. *J. Power Sources* **2016**, *310*, 26–31.
- (12) Dou, X.; Buchholz, D.; Weinberger, M.; Diemant, T.; Kaus, M.; Indris, S.; Behm, R. J.; Wohlfahrt-Mehrens, M.; Passerini, S. Study of the Na Storage Mechanism in Silicon Oxycarbide—Evidence for Reversible Silicon Redox Activity. *Small Methods* **2019**, *3* (4), 1800177.
- (13) Komaba, S.; Matsuura, Y.; Ishikawa, T.; Yabuuchi, N.; Murata, W.; Kuze, S. Redox Reaction of Sn-Polyacrylate Electrodes in Aprotic Na Cell. *Electrochem. Commun.* **2012**, *21*, 65–68.
- (14) Dou, X.; Hasa, I.; Saurel, D.; Vaalma, C.; Wu, L.; Buchholz, D.; Bresser, D.; Komaba, S.; Passerini, S. Hard Carbons for Sodium-Ion Batteries: Structure, Analysis, Sustainability, and Electrochemistry. *Mater. Today* **2019**, *23*, 87–104.
- (15) Dou, X.; Hasa, I.; Saurel, D.; Jauregui, M.; Buchholz, D.; Rojo, T.; Passerini, S. Impact of the Acid Treatment on Lignocellulosic Biomass Hard Carbon for Sodium-Ion Battery Anodes. *ChemSusChem* **2018**, *11* (18), 3276–3285.
- (16) Wahid, M.; Puthusseri, D.; Gawli, Y.; Sharma, N.; Ogale, S. Hard Carbons for Sodium-Ion Battery Anodes: Synthetic Strategies,

Material Properties, and Storage Mechanisms. *ChemSusChem* **2018**, *11* (3), 506–526.

(17) Guo, S.; Yi, J.; Sun, Y.; Zhou, H. Recent Advances in Titanium-Based Electrode Materials for Stationary Sodium-Ion Batteries. *Energy Environ. Sci.* **2016**, *9* (10), 2978–3006.

(18) Zhang, W.; Luo, N.; Huang, S.; Wu, N.-L.; Wei, M. Sulfur-Doped Anatase TiO<sub>2</sub> as an Anode for High-Performance Sodium-Ion Batteries. *ACS Appl. Energy Mater.* **2019**, *2* (5), 3791–3797.

(19) Xu, Z.-L.; Lim, K.; Park, K.-Y.; Yoon, G.; Seong, W. M.; Kang, K. Engineering Solid Electrolyte Interphase for Pseudocapacitive Anatase TiO<sub>2</sub> Anodes in Sodium-Ion Batteries. *Adv. Funct. Mater.* **2018**, *28* (29), 1802099.

(20) Tahir, M. N.; Oschmann, B.; Buchholz, D.; Dou, X.; Lieberwirth, I.; Panthöfer, M.; Tremel, W.; Zentel, R.; Passerini, S. Extraordinary Performance of Carbon-Coated Anatase TiO<sub>2</sub> as Sodium-Ion Anode. *Adv. Energy Mater.* **2016**, *6* (4), 1501489.

(21) Wu, L.; Bresser, D.; Buchholz, D.; Giffin, G. A.; Castro, C. R.; Ochel, A.; Passerini, S. Unfolding the Mechanism of Sodium Insertion in Anatase TiO<sub>2</sub> Nanoparticles. *Adv. Energy Mater.* **2015**, *5* (2), 1401142.

(22) Witkowska, A.; Di Cicco, A.; Principi, E. Local Ordering of Nanostructured Pt Probed by Multiple-Scattering XAFS. *Phys. Rev. B: Condens. Matter Mater. Phys.* **2007**, *76* (10), 104110.

(23) Greco, G.; Witkowska, A.; Principi, E.; Minicucci, M.; Di Cicco, A. Local Structural and Chemical Ordering of Nanosized Pt 3 ± δ Co Probed by Multiple-Scattering x-Ray Absorption Spectroscopy. *Phys. Rev. B: Condens. Matter Mater. Phys.* **2011**, *83* (13), 134103.

(24) Filipponi, A.; Di Cicco, A.; Natoli, C. R. X-Ray-Absorption Spectroscopy and *n*-Body Distribution Functions in Condensed Matter. I. Theory. *Phys. Rev. B: Condens. Matter Mater. Phys.* **1995**, *52* (21), 15122–15134.

(25) Filipponi, A.; Di Cicco, A. X-Ray-Absorption Spectroscopy and *n*-Body Distribution Functions in Condensed Matter. II. Data Analysis and Applications. *Phys. Rev. B: Condens. Matter Mater. Phys.* **1995**, *52* (21), 15135–15149.

(26) Holzwarth, U.; Gibson, N. The Scherrer Equation versus the “Debye-Scherrer Equation”. *Nat. Nanotechnol.* **2011**, *6* (9), 534–534.

(27) Kammel, M.; Wiedenmann, A.; Hoell, A. Nuclear and Magnetic Nanostructure of Magnetite Ferrofluids Studied by SANS POL. *J. Magn. Magn. Mater.* **2002**, *252*, 89–91.

(28) Ruland, W. IUCr. Small-Angle Scattering of Two-Phase Systems: Determination and Significance of Systematic Deviations from Porod’s Law. *J. Appl. Crystallogr.* **1971**, *4* (1), 70–73.

(29) Wu, Z. Y.; Ouvrard, G.; Gressier, P.; Natoli, C. R. Ti and O K Edges for Titanium Oxides by Multiple Scattering Calculations: Comparison to XAS and EELS Spectra. *Phys. Rev. B: Condens. Matter Mater. Phys.* **1997**, *55* (16), 10382–10391.

(30) Frenkel, A. I.; Hills, C. W.; Nuzzo, R. G. A View from the Inside: Complexity in the Atomic Scale Ordering of Supported Metal Nanoparticles. *J. Phys. Chem. B* **2001**, *105*, 12689–12703.

(31) Farges, F.; Brown, G. E.; Rehr, J. J. Ti K -Edge XANES Studies of Ti Coordination and Disorder in Oxide Compounds: Comparison between Theory and Experiment. *Phys. Rev. B: Condens. Matter Mater. Phys.* **1997**, *56* (4), 1809–1819.

(32) Vlais, G.; Bart, J. C. J.; Cavignolo, W.; Mobilio, S.; Navarra, G. EXAFS Study of Rutile and Anatase. *Z. Naturforsch., A: Phys. Sci.* **1981**, *36* (11), 1192–1195.

(33) Grunes, L. A. Study of the K Edges of 3 d Transition Metals in Pure and Oxide Form by X-Ray-Absorption Spectroscopy. *Phys. Rev. B: Condens. Matter Mater. Phys.* **1983**, *27* (4), 2111–2131.

(34) Lutterotti, L. Maud: A Rietveld Analysis Program Designed for the Internet and Experiment Integration. *Acta Crystallogr., Sect. A: Found. Crystallogr.* **2000**, *A56*, s54.

(35) MATSUO, S.; SAKAGUCHI, N.; WAKITA, H. Pre-Edge Features of Ti K-Edge X-Ray Absorption Near-Edge Structure for the Local Structure of Sol-Gel Titanium Oxides. *Anal. Sci.* **2005**, *21* (7), 805–809.

(36) Sturge, M. D. The Jahn-Teller Effect in Solids. *Solid State Phys.* **1968**, *20*, 91–211.

(37) Jahn, H. A.; Teller, E. Stability of Polyatomic Molecules in Degenerate Electronic States - I—Orbital Degeneracy. *Proc. R. Soc. London. Ser. A - Math. Phys. Sci.* **1937**, *161* (905), 220–235.

(38) Kavan, L.; Kalbáč, M.; Zúkalová, M.; Exnar, I.; Lorenzen, V.; Nesper, R.; Graetzel, M. Lithium Storage in Nanostructured TiO<sub>2</sub>Made by Hydrothermal Growth. *Chem. Mater.* **2004**, *16* (3), 477–485.

(39) Khramov, E.; Kotolevich, Y.; García Ramos, J. C.; Pestryakov, A.; Zubavichus, Y.; Bogdanchikova, N. Amorphization of Degussa Nanosized TiO<sub>2</sub> Caused by Its Modification. *Fuel* **2018**, *234*, 312–317.

(40) González, J. R.; Alcántara, R.; Nacimiento, F.; Ortiz, G. F.; Tirado, J. L. Microstructure of the Epitaxial Film of Anatase Nanotubes Obtained at High Voltage and the Mechanism of Its Electrochemical Reaction with Sodium. *CrystEngComm* **2014**, *16* (21), 4602–4609.

(41) Eshetu, G. G.; Grugeon, S.; Kim, H.; Jeong, S.; Wu, L.; Gachot, G.; Laruelle, S.; Armand, M.; Passerini, S. Comprehensive Insights into the Reactivity of Electrolytes Based on Sodium Ions. *ChemSusChem* **2016**, *9* (5), 462–471.

(42) Bresser, D.; Paillard, E.; Binetti, E.; Krueger, S.; Striccoli, M.; Winter, M.; Passerini, S. Percolating Networks of TiO<sub>2</sub> Nanorods and Carbon for High Power Lithium Insertion Electrodes. *J. Power Sources* **2012**, *206*, 301–309.

(43) Zachau-Christiansen, B.; West, K.; Jacobsen, T.; Atlung, S. Lithium Insertion in Different TiO<sub>2</sub>Modifications. *Solid State Ionics* **1988**, *28–30*, 1176–1182.

(44) Kavan, L.; Grätzel, M.; Gilbert, S. E.; Klemenz, C.; Scheel, H. J. Electrochemical and Photoelectrochemical Investigation of Single-Crystal Anatase. *J. Am. Chem. Soc.* **1996**, *118* (28), 6716–6723.

(45) Wagemaker, M.; Borghols, W. J. H.; Mulder, F. M. Large Impact of Particle Size on Insertion Reactions. A Case for Anatase Li<sub>x</sub>TiO<sub>2</sub>. *J. Am. Chem. Soc.* **2007**, *129* (14), 4323–4327.

(46) Wagemaker, M.; Kearley, J. G.; van Well, A. A.; Mutka, H.; Mulder, F. M. Multiple Li Positions inside Oxygen Octahedra in Lithiated TiO<sub>2</sub> Anatase. *J. Am. Chem. Soc.* **2003**, *125* (3), 840–848.

(47) Ohzuku, T.; Kodama, T.; Hirai, T. Electrochemistry of Anatase Titanium Dioxide in Lithium Nonaqueous Cells. *J. Power Sources* **1985**, *14* (1–3), 153–166.

(48) Wan, J.; Chen, W.; Jia, C.; Zheng, L.; Dong, J.; Zheng, X.; Wang, Y.; Yan, W.; Chen, C.; Peng, Q.; Wang, D.; Li, Y. Defect Effects on TiO<sub>2</sub> Nanosheets: Stabilizing Single Atomic Site Au and Promoting Catalytic Properties. *Adv. Mater.* **2018**, *30* (11), 1705369.

(49) Krumrey, M.; Ulm, G. High-Accuracy Detector Calibration at the PTB Four-Crystal Monochromator Beamline. *Nucl. Instrum. Methods Phys. Res., Sect. A* **2001**, *467–468*, 1175–1178.

(50) Gerlach, M.; Krumrey, M.; Cibik, L.; Müller, P.; Rabus, H.; Ulm, G. Cryogenic Radiometry in the Hard X-Ray Range. *Metrologia* **2008**, *45* (5), 577–585.

(51) Breßler, I.; Kohlbrecher, J.; Thünemann, A. F. IUCr. SASfit: A Tool for Small-Angle Scattering Data Analysis Using a Library of Analytical Expressions. *J. Appl. Crystallogr.* **2015**, *48* (5), 1587–1598.

(52) Wojdyr, M. Fityk: A General-Purpose Peak Fitting Program. *J. Appl. Crystallogr.* **2010**, *43* (5), 1126–1128.

(53) Krause, M. O.; Oliver, J. H. Natural Widths of Atomic K and L Levels, K $\alpha$  X-ray Lines and Several K L L Auger Lines. *J. Phys. Chem. Ref. Data* **1979**, *8* (2), 329–338.